Carbon 99 (2016) 318–329

Contents lists available at ScienceDirect

Carbon

journal homepage: www.elsevier.com/locate/carbon

Smaller particle size and higher oxidation improves biocompatibility of graphene-based materials

Artur M. Pinto [a, b, c], Carolina Gonçalves [a], Daniela M. Sousa [b, c], Ana R. Ferreira [b, c], J. Agostinho Moreira [d], Inês C. Gonçalves [b, c, **, 1], Fernão D. Magalhães [a, *, 1]

[a] LEPABE, Faculdade de Engenharia, Universidade do Porto, Rua Dr. Roberto Frias, 4200-465 Porto, Portugal
[b] INEB – Instituto de Engenharia Biomédica, Universidade do Porto, Rua do Campo Alegre, 823, 4150-180 Porto, Portugal
[c] Instituto de Investigação e Inovação em Saúde, Universidade do Porto, Portugal
[d] IFIMUP and IN – Institute of Nanoscience and Nanotechnology, Departamento de Física e Astronomia, Faculdade de Ciências, Universidade do Porto, Rua do Campo Alegre 687, 4169-007, Porto, Portugal

ARTICLE INFO

Article history:
Received 7 April 2015
Received in revised form
26 November 2015
Accepted 30 November 2015
Available online 15 December 2015

ABSTRACT

Graphene-based materials (GBMs) have recognized potential for biomedical applications, however different production methods and treatments originate divergent biocompatibility. In this work, two commercially available graphene nanoplatelets (GNP) were studied, differing in platelet size: GNP-C, with 1–2 μm, and GNP-M, with 5 μm. GNP-M was oxidized using $KMnO_4$ in different ratios (1:3 and 1:6), leading to GNP-M-ox-1:3 and GNP-M-ox-1:6. The effect of oxidation and size on biocompatibility was evaluated *in vitro*. Hemolysis was below 3% for all GBMs from 100 to 500 μg mL^{-1}. GNP-C entered human fibroblasts (HFF-1) inducing reactive oxygen species production after 1 h for 10 μg mL^{-1}, leading to metabolic activity decreases at 24 h, which reverted at 48 h and 72 h. GNP-C was toxic to HFF-1 for 50 μg mL^{-1}. Despite that, GNP-C did not cause damages on cell membrane, opposed to GNP-M and GNP-M-ox-1:3, which were toxic for 20 μg mL^{-1}. GNP-M-ox-1:6 did not decrease metabolic activity or cause membrane damages until 100 μg mL^{-1} (highest tested) for 72 h. This is explained by complete oxidation causing folding of GNP-M sharp edges, therefore preventing damages. Thus, GNP-M-ox-1:6 has potential for biomedical applications. Equivalent metabolic activity results were obtained for all materials with HPMEC (Human Pulmonary Microvascular Endothelial Cells).

1. Introduction

Graphene is a single layer of sp^2 carbon atoms arranged in a honeycomb structure. It possesses very high mechanical strength, specific surface area and high thermal and electrical conductivity [1–9]. Strong oxidizing agents can be used to produce oxidized forms of graphene, designated as graphene oxide (GO). Also, graphite can be directly oxidized to produce graphite oxide, which can then be exfoliated originating GO [4]. The presence of polar and reactive oxygen-containing functional groups in graphene oxide [10–15] reduces its thermal stability, but may be important to promote interaction and compatibility with polar solvents and with some polymer matrices [4,8,16–18].

Several biomedical applications have been studied for graphene-based materials (GBMs), like biosensing/bioimaging [19], drug delivery [18], cancer photothermal therapy [20], regenerative medicine [21,22], and antibacterial materials [18]. Examples of GBMs functions in some of the mentioned fields are: a) improvement of biomaterials mechanical/electrical properties, b) adsorption and targeted delivery of drugs, c) strong optical absorption of near infrared radiation, d) increase of cellular attachment and growth at biomaterials surface, and e) induction of selective damages in bacteria. In view of the growing interest in using GBMs in medical applications, it is relevant to evaluate their biocompatibility. From existent studies it can be concluded that generally GBMs induce a decrease on cell viability above a concentration of 10 μg mL^{-1} after 24 h incubation, with cell viability often decreasing with time and concentration. GBMs interaction with cells depends on their intrinsic physical––chemical properties (*e.g.* size, hydrophilicity), which are related to the raw materials and

* Corresponding author.
** Corresponding author. INEB – Instituto de Engenharia Biomédica, Universidade do Porto, Rua do Campo Alegre, 823, 4150-180 Porto, Portugal.
E-mail addresses: icastro@ineb.up.pt (I.C. Gonçalves), fdmagalh@fe.up.pt (F.D. Magalhães).
[1] Both authors contributed equally to this work.

http://dx.doi.org/10.1016/j.carbon.2015.11.076
0008-6223/

production methods used. However, few studies are available and some contradictory results can be found in literature. This subject was recently reviewed by Pinto et al. [23,24]. There is still the need to perform a comprehensive characterization for the different GBMs available, in terms of both physical–chemical properties and biocompatibility. Also, since several biomedical applications under study for GBMs imply contact with blood, hemocompatibility studies are necessary to assess the clinic safety of intravenous administration or implantation of GBMs [23,24]. Some GBMs have been reported to induce cell death by different mechanisms: a) generation of reactive oxygen species (ROS), which leads to lipid peroxidation, denaturation of proteins, DNA degradation, and activation of apoptosis, b) direct damage on cell membrane by a blade-like action of the particles sharp edges [25], c) decrease of free cell surface area modifying metabolic changes with the cell medium, leading to poor nutrient absorption and inefficient waste release, or affecting cell–cell interaction [26]. Thus, careful characterization of each particular GBM is needed to assure their biocompatibility.

The present work studies a commercially available product, with reduced cost comparing with single layer graphene: graphene nanoplatelets (GNP). Each particle is constituted by at least 2 stacked graphene layers, possessing oxygen-containing functional groups at the edges. Since this is a commercial product, there is the advantage of material consistency and availability. Moreover, GNP has been reported to display good results as biopolymers fillers, improving mechanical performance [24] and biocompatibility, namely reducing platelets activation without increasing toxicity [24]. In this work, the biocompatibility of GNP is studied for different sizes and oxidation states. Namely, evaluating hemolysis, effects on cell viability, proliferation, mitochondrial membrane potential and morphology, and ROS production.

2. Materials and methods

2.1. Graphene-based materials oxidation

Graphene nanoplatelets (GNP) grades M5 and C750, were acquired from XG Sciences (Lansing, USA), with the following characteristics: Grade M5 (GNP-M) – average thickness of 6–8 nm, maximum length 5 μm, and surface area between 120 and 150 $m^2\ g^{-1}$; Grade C750 (GNP-C) – average thickness lower than 2 nm and surface area of 750 $m^2\ g^{-1}$. The sizes of a typical grade C sample has a distribution that ranges from very small flakes (diameter below 100 nm) up to larger flakes (1–2 μm). According to the manufacturer, GNP production is based on exfoliation of sulphuric acid-based intercalated graphite by rapid microwave heating, followed by ultrasonic treatment [27].

GNP-M was oxidized by modified Hummers method (MHM), as described in our previous work [24]. Briefly, 50 mL of H_2SO_4 were added to 2 g of GNP-M at room temperature and the solution was cooled using an ice bath, followed by gradual addition of $KMnO_4$, 6 g for GNP-M-ox-1:3 and 12 g for GNP-M-ox-1:6. Then 300 mL of distilled water were added, followed by addition of H_2O_2 until oxygen release stopped. GNP-M-ox-1:3 and 1:6 were washed 5 times with water by centrifugation at 4000 rpm during 15 min. The solids were dispersed in 500 mL of water by sonication (Bandelin Sonorex R K512 H) during 5 h, frozen at −80 °C and lyophilized for 72 h.

2.2. GBMs physical-chemical characterization

2.2.1. GBMs physical characterization

2.2.1.1. Scanning electron microscopy (SEM). The morphology of GBMs was observed using SEM (FEI Quanta 400FEG, with acceleration voltage of 3 kV). Powders of the nanomaterials were applied on conductive carbon strips for visualization.

2.2.1.2. Dynamic light scattering. Particle sizes and distributions of the materials were determined with an LS230 laser particle analyzer (Coulter, USA). GBMs were dispersed in water at a concentration of 100 μg mL^{-1} and sonicated for 1 h. Just before sample testing, 10 min sonication was performed to redisperse agglomerates using a Bandelin Sonorex R K512 H ultrasound bath. Data were collected performing 3 scans of 60 s, including polarization intensity differential scattering and using Fraunhofer's model. This model assumes spherical shape for the particles in suspension. The obtained size distributions must therefore be considered as relative evaluations of the degree of deagglomeration of the different materials in water, and not as precise estimations of particle sizes. Li et al. [28] used a similar approach to evaluate graphene oxide particle size distribution in water by dynamic light scattering.

2.2.2. GBMs chemical characterization

2.2.2.1. X-ray photoelectron spectroscopy (XPS). The XPS analysis of GBMs powders tablets (d = 10 mm) was performed at CEMUP (Centro de Materiais da Universidade do Porto) using a ESCALAB 200A, VG Scientific (UK) with PISCES software for data acquisition and analysis. For analysis, an achromatic Al (Kα) X-ray source (1486.6 eV) operating at 15 kV (300 W) was used, and the spectrometer, calibrated with reference to Ag $3d_{5/2}$ (368.27 eV), was operated in constant analyser energy mode with a pass energy of 20 eV for regions of interest, and 50 eV in survey. The core levels for O 1s and C 1s were analyzed. The photoelectron take-off angle (the angle between the surface of the sample and the axis of the energy analyzer) was 90°. The electron gun used focused on the specimen in an area close to 100 mm^2. Data acquisition was performed with a pressure lower them 1×10^6 Pa. The effect of the electric charge was corrected by the reference of the carbon peak (285 eV). The deconvolution of spectra was performed with the XPSPEAK41 program, in which a peak fitting was performed using Gaussian–Lorentzian peak shape and Shirley type background subtraction.

2.2.2.2. Raman spectroscopy. The unpolarized Raman spectra of GNP-C, GNP-M, GNP-M-ox-1:3 and GNP-M-ox-1:6 powders were obtained under ambient conditions, in several positions for each sample. The linear polarized 514.5 nm line of an Ar^+ laser was used as excitation. The Raman spectra were recorded in a backscattering geometry by using a confocal Olympus BH-2 microscope with a 50× objective. The spatial resolution is about 2 μm, and laser power was 15 mW. The scattered radiation was analysed using a Jobin–Yvon T64000 triple spectrometer, equipped with a charge-coupled device. The analysis diameter was 10 μm and spectral resolution was better than 4 cm^{-1}.

The spectra were quantitatively analysed by fitting a sum of damped oscillator to the experimental data, according to the equation:

$$I(\omega,T) = B(\omega) + (1 + n(\omega,T)) \sum_{j=1}^{N} A_{oj} \frac{\omega \Omega_{oj}^2 \Gamma_{oj}}{\left(\Omega_{oj}^2 - \omega^2\right)^2 + \omega^2 \Gamma_{oj}^2} \qquad (1)$$

Here $n(\omega,T)$ is the Bose-Einstein factor: A_{oj}, Ω_{oj} and Γ_{oj} are the strength, wave number and damping coefficient of the j-th oscillator, respectively, and $B(\omega)$ is the background. In this work, the background was well simulated by a linear function of the frequency, which enable us to obtain reliable fits of Equation (1) to the experimental data. The fitting procedure was performed for all Raman bands collected from the same sample, but in different

positions. This procedure allows us to determine the average and standard deviation (SD) values of the phonon parameters, namely the wave number and intensity [29].

2.2.2.3. Thermogravimetric analysis (TGA). Thermal stability of samples was determined with a Netzsh STA 449 F3 Jupiter device. Sample amounts ranged from 10 to 12 mg. The thermograms were recorded between 50 and 800 °C at a heating rate of 10 °C min^{-1} under nitrogen flow.

2.3. GBMs biocompatibility

GBMs were sterilized in ethanol by dispersion and sonication during 20 min (Bandelin Sonorex RK 512 H). Materials were dried in a vacuum oven overnight at 50 °C under sterile conditions. GBMs were redispersed in appropriate volume of phosphate buffered saline (PBS, pH 7.4) or cell culture medium.

2.3.1. Hemolysis assay

Red blood cells (RBCs) were isolated from buffy coats (obtained from Immunohemotherapy Service, Hospital S. João, Porto, Portugal), as described previously [30]. Briefly, RBCs were centrifuged over density gradient with Histopaque-1077 (Sigma–Aldrich) according to the manufacturer's instructions. After removal of the plasma upper layer, the lower layer containing RBC was washed three times in PBS. The purified RBCs were diluted to a concentration of 2×10^8 cells mL^{-1} and 100 μL of RBCs were placed in round bottom 96 wells polypropylene microtiter plates. Next, 100 μL of GNP dispersions were added to the wells and incubated for 3 h at 37 °C and 80 rpm. Afterwards, 96-well plates were centrifuged at 4000 rpm for 15 min to collect supernatant, which was transferred (80 μL) from each well to black polypropylene 96 wells microtiter plates for absorbance reading. Absorbance was read at 380, 415, and 450 nm using a micro-plate reader spectrophotometer (Bioteck Plate Reader, Synergy MX). The amount of hemoglobin (Hb) is calculated as follows: Hb value of sample (mg dL^{-1}) = [[2 × A_{415} − (A_{380} + A_{450})] × 1000 × Dilution factor]/(E), where A_{415}, A_{380}, A_{450} are the absorbance values at 415, 380, and 450 nm, respectively. A_{415} is the Soret band absorption of Hb and A_{380}, A_{450} are correction factors of uroporphyrin whose absorption falls under the same wavelength range. E is the molar absorptivity of oxyhemoglobin at 415 nm, which is 79.46. The hemolytic potential of GNP was calculated as follows: Hemolysis (%) = Hb value of sample/Total Hb value × 100, where total Hb value corresponds to 100% hemolysis with Triton 1% (Sigma Aldrich, X100) [31]. GBMs concentrations tested were 100, 200 and 500 μg mL^{-1}. Controls with PBS (lysis negative control) and Triton 1% in PBS (positive control for 100% hemolysis) were performed. Additionally, controls with only GBMs in PBS were performed for each concentration tested. All assays were performed in triplicate and repeated 3 times.

2.3.2. Biocompatibility with cell line

Human foreskin fibroblasts HFF-1 (from ATCC) where grown in DMEM+ (Dulbecco's modified Eagle's medium (DMEM, Gibco) supplemented with 10% (V/V) foetal bovine serum (Gibco) and 1% (V/V) penicillin/streptomycin (biowest) at 37 °C, in a fully humidified air containing 5% CO_2. The media were replenished every 3 days. When reaching 90% confluence, cells were rinsed with PBS (37 °C) and detached from culture flasks (TPP®) using 0.25% (w/V) trypsin solution (Sigma Aldrich) in PBS. For all assays, HFF-1 cells were seeded at a density of 2×10^4 cells mL^{-1} in 96 well plates or in 8 chamber Lab-Tek-II. Upon subconfluence (24 h), DMEM+ was removed and cells incubated with increasing concentrations of GBMs in DMEM+ (1–100 μg mL^{-1}) for 24, 48, and 72 h. At indicated time-points, cells were observed in an inverted fluorescence microscope (Carl Zeiss – Axiovert 200) and phase contrast images were acquired. All experiments were performed using cells between passages 10 to 14.

HPMEC-ST1.6R cells (from ATCC) were cultured in culture flasks (TPP®) treated with 0.2% gelatine (Sigma) in medium M199+ (M199 medium (Sigma–Aldrich) supplemented (M199+) with 20% (V/V) foetal bovine serum (FBS), 2 mM Glutamax I, 100 U/100 μg mL^{-1} Pen/Strep, (all Gibco Invitrogen), 25 μg mL^{-1} sodium heparin (Sigma–Aldrich), 25 μg mL^{-1} endothelial cell growth supplement (ECGS, Becton Dickinson), and 50 μg mL^{-1} G-418 (Gibco, Invitrogen). For resazurin assay, HPMEC cells were seeded at a density of 2×10^4 cells mL^{-1} in 96 well plates coated with 0.2% gelatine. Upon subconfluence (24 h), M199+ was removed and cells incubated with increasing concentrations of GBMs in M199+ (10–100 μg mL^{-1}) for 24, and 72 h. At indicated time-points, cells were observed in an inverted fluorescence microscope (Carl Zeiss – Axiovert 200) and phase contrast images were acquired. All experiments were performed using cells between passages 26 to 37.

2.3.3. Cytotoxicity assays

Cell metabolic activity was quantified by resazurin assay at 24, 48, and 72 h of incubation. Briefly, 20 μL (1 mg mL^{-1}) resazurin (Sigma Aldrich) solution in PBS was added to each well. Cells were incubated for 3 h and fluorescence ($\lambda_{ex/em}$ = 530/590 nm) read in a micro-plate reader spectrophotometer. Negative control for metabolic activity decrease was performed incubating cells with DMEM+ and positive control incubating with Triton 0.1 wt.%. Cell metabolic activity (%) was calculated as follows: Fluorescence of sample/Fluorescence of negative control * 100. Controls were performed with materials only (without cells) dispersed in DMEM+, for all concentrations tested. All assays were performed in sextuplicate and repeated 3 times.

Cell viability/membrane integrity was evaluated by LIVE/DEAD assay. Hoechst 33342 permeates membrane and stains nucleic acids. Calcein also permeates membrane and is metabolized in cytoplasm by intracellular esterases originating a green highly fluorescent derivative. Cell membrane has residual permeability to propidium iodide, which only enters cells whose membrane integrity is compromised, staining nucleic acids. At 24, 48 and 72 h DMEM+ was removed and cells incubated with Hoechst 33342 (Molecular Probes) and Calcein (Molecular Probes), both at 2.5 μg mL^{-1} in PBS for 15 min, at 37 °C in the dark. Then, propidium iodide (PI) (Sigma Aldrich) in PBS was added to each well to a final concentration of 1.25 μg mL^{-1} and images acquired in an inverted fluorescence microscope (Carl Zeiss – Axiovert 200). Cell death (%) was calculated as follows: number of cells stained with PI/number of cells stained with Hoechst 33342 * 100. All assays were performed in triplicate and repeated 3 times.

TMRE (tetramethylrhodamine, ethyl ester) Mitochondrial Membrane Potential (MMP) Assay Kit (Abcam, ab113852) was used to measure MMP of HFF-1 cells according to manufacturer's instructions. HFF-1 cells were seeded in 96-well plates and exposed to GBMs at concentrations from 10 to 100 μg mL^{-1}, for 48 h. Then, cells were rinsed 3× with DMEM+ to assure no interference from materials in fluorescence determination and were loaded with 500 nM TMRE in DMEM+ for 30 min at 37 °C. Cells were rinsed once with BSA 0.2 wt.% in PBS and fluorescence ($\lambda_{ex/em}$ = 549/575 nm) read in a micro-plate reader spectrophotometer. Negative control for MMP decrease was performed with cells cultured in culture medium (DMEM+), as positive control for MMP decrease cells were exposed to carbonyl cyanide *m*-chlorophenylhydrazone (CCCP) 20 μM for 15 min. MMT (%) was calculated as follows: Fluorescence of sample/Fluorescence of negative control for MMP decrease * 100. Controls were performed with materials only (without cells) dispersed in DMEM+ for all concentrations tested

and revealed similar fluorescence to DMEM+. All assays were performed in triplicate and repeated 3 times. Cells were prepared for image acquisition in an inverted fluorescence microscope (Carl Zeiss – Axiovert 200), following the same procedure, but incubating with 500 nM TMRE and Hoechst 33342 (2.5 μg mL^{-1}), to allow observation of cell nuclei on cells with decreased MMP.

2.3.4. Intracellular ROS evaluation

Chloromethyl-2′,7′-dichlorodihydrofluorescein diacetate (CM-H_2DCFDA) is a chloromethyl derivative of H_2DCFDA, useful as an indicator for reactive oxygen species (ROS) in cells. It passively diffuses into cells, where its acetate groups are cleaved by intracellular esterases originating a highly fluorescent derivative (DCF) and its thiol-reactive chloromethyl group reacts with intracellular glutathione and other thiols. The fluorescence intensity is proportional to the ROS levels within the cell cytosol.

HFF-1 cells were seeded as previously described and, after reaching a state of subconfluence (24 h), washed with PBS at 37 °C and incubated 45 min at 37 °C with 95 μL CM-DCFH-DA (Molecular Probes) at a concentration of 2 μg mL^{-1}. The reagent was removed and cells incubated at 37 °C for 1 h, with 150 μL GBMs dispersed in PBS (1, 10, and 50 μg mL^{-1}). Finally, 100 μL Triton 1% in PBS was added to each well and fluorescence ($\lambda_{ex/em}$ = 480/530 nm) read in a micro-plate reader spectrophotometer. Controls were performed with GBMs dispersed in PBS, for all concentrations tested, incubated with the same amount of CM-H_2DCFDA, in wells without cells. PBS was used as negative control and H_2O_2 (Merck) 100 mM as positive control for intracellular ROS levels increase. ROS levels were calculated as follows: ROS levels (%) = Fluorescence of the sample/Fluorescence of negative control * 100. All assays were performed in triplicate and repeated 3 times.

2.3.5. Immunocytochemistry

Cells in each well exposed to 50 μg mL^{-1} of GBMs (at 100 μg mL^{-1} GBMs interfere with staining and images had worse quality) were washed with PBS. Then, fixation was performed with paraformaldehyde (PFA – Merck) 4 wt.% in PBS for 15 min. PFA was removed, cells washed with PBS and stored at 4 °C. Cell cytoskeletal filamentous actin can be visualized by binding of fluorescent phalloidin and the nucleus can be stained with 4′,6-Diamidino-2-phenylindole dihydrochloride (DAPI) that intercalates with nucleic acids. Cell membrane was permeabilized with Triton 0.1 wt.% at 4 °C for 5 min. Washing was done with PBS and incubation performed with phalloidin (Alexa Fluor 488; Molecular Probes) solution in PBS in a 1:80 dilution for 20 min in the dark. After rinsing with PBS, DAPI (Sigma Aldrich) solution at 3 μg mL^{-1} was added to each well and incubated for 15 min in the dark. Finally, cells were washed and kept in PBS to avoid drying. Plates with adherent cells were observed in an inverted fluorescence microscope (Carl Zeiss – Axiovert 200).

For evaluation of cell proliferation, Ki-67 immunocytochemistry was performed. Fixed and permeabilized cells were incubated with a blocking solution 4 wt.% BSA and 1% (V/V) FBS for 1 h, and subsequently incubated with rabbit anti-Ki67 primary antibody (1:100) from Abcam (ab15580) overnight. Cells were further incubated with the secondary antibody goat anti-rabbit IgG Alexa Fluor® 488 (1:800) from Invitrogen (a11070) for 1 h. Nuclei were stained with Nuclear Mask (Invitrogen, H10294). In order to identify possible nonspecific labelling, a negative control was performed excluding the incubation with primary antibody. Images were acquired using the In cell analyser 2000 6E Healthcare, equipped with an Nikon 10×/0.45 Plan Apo. Image analysis/Ki67 quantification was performed using the software In cell investigator developer toll box (GE Healthcare). Ki67 positive ($Ki67^+$) cells percentage were calculated as follows: $Ki67^+$(%) = $Ki67^+$ cells/total cell number × 100.

2.3.6. Transmission electron microscopy (TEM)

After 72 h incubation, cells exposed to 100 μg mL^{-1} GBMs in Lab-Tek-II were fixed in 2% glutaraldehyde (Electron Microscopy sciences, Hatfield, USA) and 4% PFA in cacodylate Buffer 0.1 M (pH 7.4), dehydrated and embedded in Epon resin (TAAB, Berks, England). Ultrathin sections (40–60 nm thickness) were prepared on a Leica Reichert SuperNOVA Ultramicrotome (Germany) using diamond knives (DDK, Wilmington, DE, USA). The sections were mounted on 200 mesh copper or nickel grids, stained with uranyl acetate and lead citrate for 15 min each, and examined under a JEOL JEM 1400 TEM (Tokyo, Japan). Images were digitally recorded using a CCD digital camera Orious 1100W (Tokyo, Japan) at the HEMS – Institute for Molecular and Cell Biology (IBMC) of the University of Porto.

2.4. Statistical analysis

Statistical analysis was performed using the software Statistical Package for the Social Sciences (SPSS 20, IBM, USA) performing Kruskal–Wallis one-way analysis of variance. Resazurin assays were analysed performing parametric analysis of variance (ANOVA) followed by post hoc tests Tamhane, Dunnett, and Games-Howell. Multiple means comparison were performed between samples to identify significant differences, which were considered for $p < 0.05$.

3. Results

3.1. GBMs physical-chemical characterization

3.1.1. Physical characterization

SEM imaging of the powders (Fig. 1) shows that GNP-C is constituted by platelets with a length bellow 2 μm and small flakes (<0.5 μm) that form agglomerates (Fig. 1(A and B)). The larger platelets have planar conformation, being constituted by few single layer sheets, while small flakes are wrinkled and possess folded edges (Fig. 1(B)). This probably occurs due to the flakes short dimensions allowing the oxygen-containing functional groups at the edges to form hydrogen bonds, distorting the sheets. GNP-M (Fig. 1(C and D)) is also constituted by agglomerated platelets. However, some agglomerates can be redispersed in liquid medium. Each platelet is formed by stacks of few individual “graphene” sheets, assuming planar conformations and presenting sharp edges. These platelets have a length of about 5 μm (Fig. 1(E and F)).

Oxidation of GNP-M changes its morphology. Both GNP-M-ox-1:3 (Fig. 1(G and H)) and GNP-M-ox-1:6 (Fig. 1(I and J)) powders have sizes similar to GNP-M, however oxidized platelets are more wrinkled and exhibit folded edges, due to formation of hydrogen bonds between intra-platelet oxygen-containing functional groups.

Fig. 2 reveals that GNP-C is constituted by considerably smaller particle sizes than GNP-M, showing two narrow peaks at 0.5 and 2 μm, while GNP-M has broad peaks at 20, 35 and 60 μm, with a particle size distribution ranging from few μm to 70 μm. GNP-M-ox-1:3 and 1:6 display broad distributions, almost unimodal, with particle sizes ranging from few to about 100 μm in the first case and 70 μm in the second. These results suggest that GNP-C is effectively exfoliated in water, presenting two populations of platelets with sizes below 2 μm, which is consistent with the SEM images. GNP-M is significantly agglomerated in water. Both, GNP-M-ox-1:3 and 1:6 are also agglomerated, despite the oxidation treatment, which may be due to formation of inter-particle hydrogen bonds that do not dissociate in aqueous medium.

3.1.2. Chemical characterization

XPS results (Fig. 3(A)) show that both GNP-M and GNP-C have a low degree of oxidation (atomic percentage of oxygen – O 1s

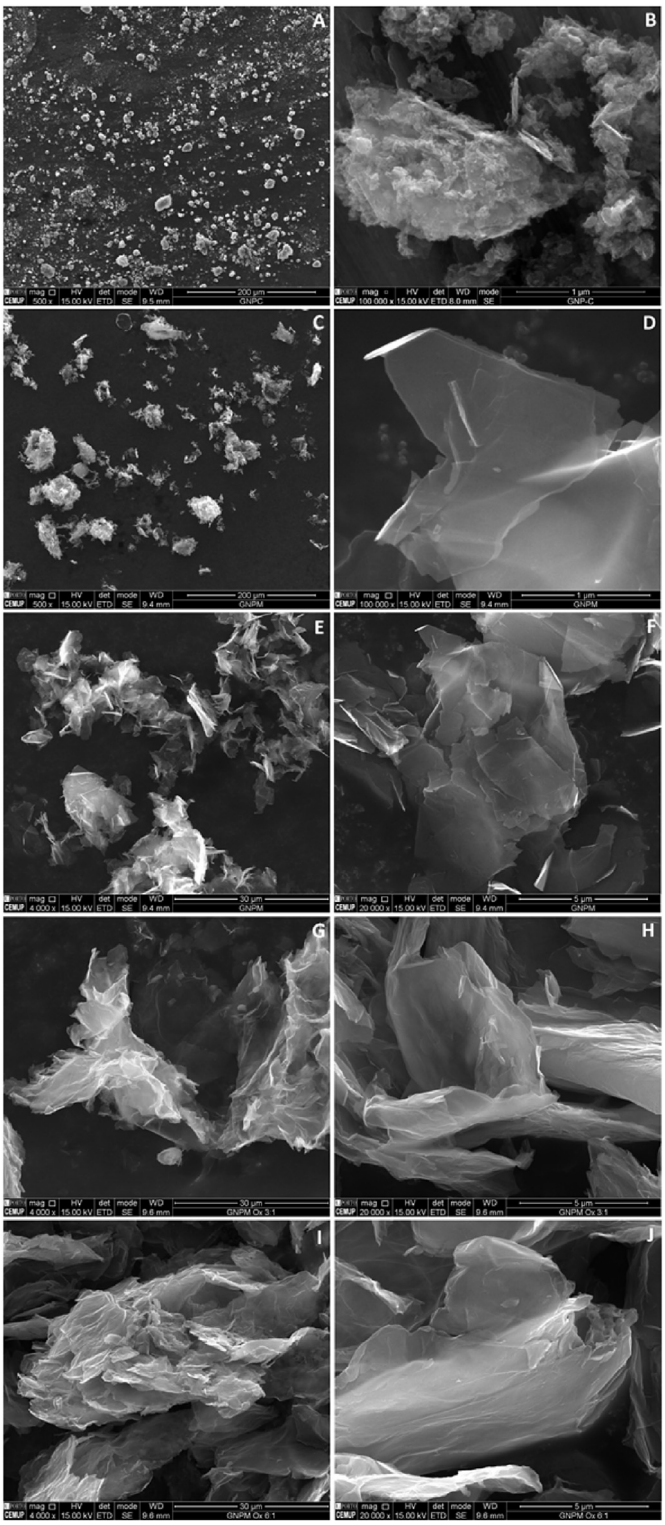

Fig. 1. SEM images of dry powders of GNP-C at (A) 500×, (B) 100000×; GNP-M at (C) 500×, (E) 4000×, (F) 20000×, and (D) 100000×; GNP-M-ox-1:3 at (G) 4000×, and (H) 20000×; and of GNP-M-ox-1:6 at (I) 4000×, and (J) 20000×.

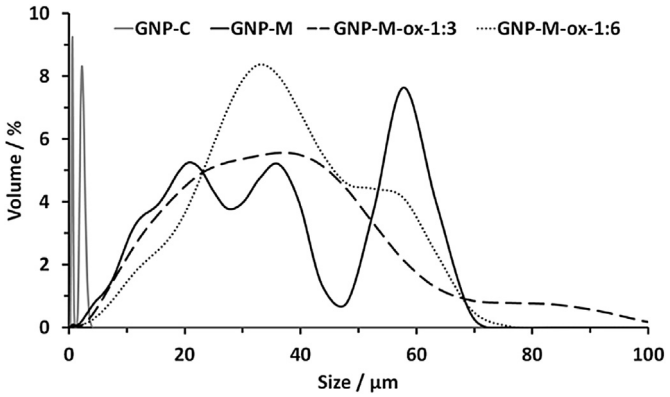

Fig. 2. Particle size distributions of GNP-C, GNP-M and GNP-M-ox-1:3 and 1:6 dispersed in water at a concentration of 100 µg mL^{-1}.

(at.%) < 4%). This was expected since GNP are obtained from graphite by microwave and ultrasonic treatment (see 2.1), and its hexagonal carbon structure should unveil defects, in the form of oxygen-containing groups, mostly at the platelet edges. XPS data also reveal that oxidation of GNP-M by modified Hummer's method, to produce GNP-M-ox-1:3 and GNP-M-ox-1:6, increases the O 1s (at.%) in the final products by about 20% (Fig. 3(A)).

Sulphuric acid (H_2SO_4) forms some epoxy groups (C—O—C) in alkenes double bonds in GNP honeycomb structure, mostly at the edges and surface defects [11]. Potassium permanganate ($KMnO_4$) also reacts with alkene double bonds (C═C) forming diols (HO—C—C—OH). However, the principal mechanism proposed for graphene oxidation by modified Hummers method is through the formation of manganese heptoxide (Mn_2O_7), which is more reactive than potassium permanganate. This strong oxidant forms carbonyls (C═O) by cleavage of alkenes double bonds. Moreover, carboxyls (HO—C═O) can be formed by further oxidation of aldehydes (H—C═O) [11]. In the formation of manganese heptoxide, sulphuric acid was used in excess and potassium permanganate was the limiting reagent. GNP-M-ox-1:6 was oxidized in presence of 2 fold the $KMnO_4$ amount comparing to GNP-M-ox-1:3. This caused strong oxidation of GNP-M-ox-1:6, probably leading to preferential formation of carboxyls (O—C═O) and hydroxyls (C—OH) (Fig. 3(A)). For GNP-M-ox-1:3, the oxidation was milder, with mostly epoxy (C—O—C) and carbonyl (C═O) groups being formed. XPS results also show that the total C—C ($sp^2 + sp^3$) is lower for GNP-M-ox-1:6, despite the total C at.% being similar for both materials. This suggests that in GNP-M-ox-1:6 the oxygen-containing functional groups are distributed by more carbon atoms than in GNP-M-ox-1:3. This statement is in agreement with what is observed in Raman results (see below), which show that GNP-M-ox-1:6 is more homogeneously oxidized than GNP-M-ox-1:3. This may be due to oxidation in GNP-M-ox-1:3 having occurred predominantly at the platelets edges. For GNP-M-ox-1:6, due to excess manganese heptoxide, oxygen-containing functional groups were also produced throughout the platelets surfaces, despite this being less sterically favourable than edge oxidation [11].

The ratio between C sp^2 and sp^3 is lower for GNP-M than for GNP-C (Fig. 3(A)), because it has higher thickness, thus more electronic delocalization trough parallel single carbon sheets. This ratio also decreases with oxidation [32], due to the induction of defects at platelets surface by cleavage of alkene double bonds and aldehydes oxidation to form carboxyls. Moreover, stronger oxidation, as observed for GNP-M-ox-1:6, leads to the lowest sp^2/sp^3 ratio. This is in agreement with this material being more homogenously oxidized.

A

Elements at.% / Chemical group	Binding Energy eV	GNP-C %	GNP-M %	GNP-M-ox-1:3 %	GNP-M-ox-1:6 %
C 1s	-	96.0	97.3	76.3	76.5
O 1s	-	4.0	2.7	23.7	23.5
C-C (sp^2)	284.6	61.2	58.3	38.9	32.3
C-C (sp^3)	285.4	38.8	41.7	32.8	30.7
C-OH	286.4	-	-	4.3	10.7
C-O-C	287.1	-	-	12.9	7.9
C=O	288.0	-	-	6.9	2.5
O-C=O	289.2	-	-	4.2	15.8
sp^2/sp^3	-	1.58	1.40	1.18	1.05

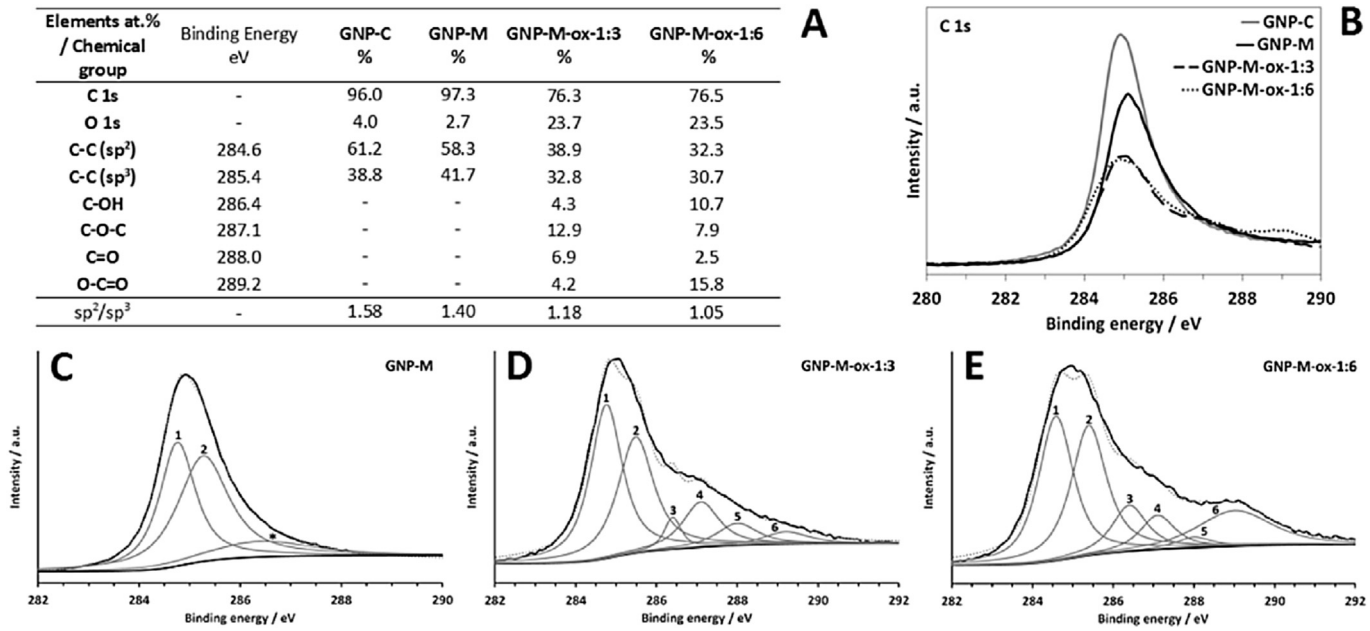

Fig. 3. A) Table shows atomic composition of GBMs and content of C 1s chemical groups resulting from spectra fitting (*fitting for oxygen groups of GNP-C and M could not be performed due to having low content); B) XPS spectra for the core level C 1s for GNP-C, M, GNP-M-ox-1:3 and 1:6; C, D, E) spectra fitting for GNP-M, GNP-M-ox-1:3 and 1:6, respectively. Deconvoluted peaks shown correspond to: 1) C=C (sp^2), 2) C–C (sp^3), 3) C–OH, 4) C–O–C, 5) C=O, and 6) O–C=O.

As seen in Fig. 4(A), Raman spectra obtained for GBMs powders are similar. D-band, located between 1270 and 1450 cm^{-1}, is assigned to the carbon lattice disorder typical of crystal edges and defects in the graphene network. G-band close to 1580 cm^{-1}, is associated with the sp^2 hybridization [33,34]. From the fitting procedure, we have calculated the intensity of the observed Raman bands. It is well established that the ratio between the intensities of the D- and G-bands, $I_{D/G}$, is widely used for characterizing the defects degree in graphene materials and to evaluate multilayered graphene crystallite size [33]. Usually, the D band is absent or week in the surface of graphene sheets and intense in their edges [34]. For this reason, the ratio between the D- and G-bands is higher for GNP-C, because it exhibits a smaller mean diameter than GNP-M, having more edges in the analysis volume.

The oxidation of GNP-M lead to an increase of D-band intensity (Fig. 4(B)), due to disruption of sp^2 hybridization in the interior of graphene sheets due to introduction of oxygen containing functional groups and also due to weakening of π interactions between individual sheets and particles [8,35]. GNP-M-ox-1:3 has a lower $I_{D/G}$ ratio, comparing with GNP-M-ox-1:6, because in some spectra acquired, D-band was intense but in other cases, this band presented an intensity similar to non oxidized GNP-M. This points out for a non-uniform oxidization when a ratio of GNP-M 1:3 $KMnO_4$ is used, as it was discussed previously (see 2.2.2.1). Opossingly, all spectra of GNP-M-ox-1:6 present an intense D-band and a broader G-band, evidencing both homogeneous and large degree of oxidation. Moreover, G band width slightly increases for both oxidized materials comparing with non-oxidized GNP-M and D band width is higher for the more oxidized GNP-M-ox-1:6 (Fig. 4(B)).

Thermograms for GBMs are shown in Fig. 4(C). GNP-C and GNP-M display similar behaviour along heating ramp, having small weight losses (GNP-C = 13.8 wt.%, GNP-M = 20.7 wt.%) mostly above 400 °C. GNP-M-ox-1:3 shows 55.5 wt.% weight loss and GNP-M-ox-1:6 68.3 wt.% after heating up to 800 °C, more 34.8 and 47.6 wt.% than pristine GNP-M, respectively. This confirms that oxidation occurred to a higher degree in GNP-M-ox-1:6 than for GNP-M-ox-1:3. Also, GNP-M-ox-1:3 earlier occurring weight loss points out the predominant location of thermolabile oxygen-containing groups at sheets edges [36,37].

3.2. GBMs biocompatibility

3.2.1. Hemolysis evaluation

Fig. 5 shows that both GNP-M (2.5%) and GNP-C (1.7%) induce low hemolysis even in concentrations up to 500 μg mL^{-1}. Despite being dark-coloured, GBMs did not interfere with measurements in Hb absorption wavelength for all concentrations tested. Materials were washed or centrifuged in order to assure the removal of possible contaminants from production/storage, however these procedures revealed unnecessary, because hemolysis was not decreased (Fig. S1).

No significant differences in hemolysis were observed between GNP-M and GNP-C for all concentrations tested ($p > 0.05$). The oxidation of GNP-M, significantly reduced hemolysis ratio for both GNP-M-ox-1:3 and 1:6 for the higher concentrations tested of 200 and 500 μg mL^{-1} (Fig. 5). As an example, for 500 μg mL^{-1}, GNP-M hemolysis was 2.5%, GNP-M-ox-1:3 0.04% and 1:6 0.08%. This can be explained by the presence of oxygen-containing functional groups at sheets edges causing folding, therefore reducing the occurrence of physical damages to cells.

3.2.2. Biocompatibility with fibroblasts

After verifying that the materials do not show relevant toxic effects towards RBCs, further assays were performed to evaluate their effect when in direct contact with human foreskin fibroblasts (HFF-1). Phase contrast images were obtained for each time and concentration tested, representative images are shown in Fig. S2. Further characterization was performed and described below.

3.2.2.1. Cytotoxicity. Considering that a sample has cytotoxic potential if its metabolic activity is reduced to less than 70% comparing to negative control for metabolic activity decrease (cells incubated with DMEM+) [ISO 10993-5:2009(E)], it can be observed from Fig. 6(A) that both GNP-M and GNP-C are potentially non-toxic up to a concentration of 20 μg mL^{-1}, until 72 h. GNP-C is

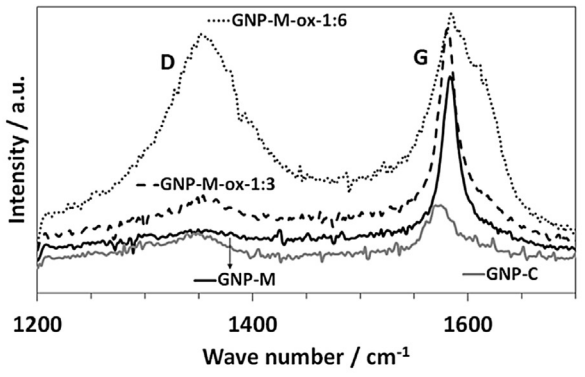

B

Samples (n=3)	$I_{(D/G)}$		$I_{Width(G)}$		$I_{Width(D)}$	
	Avr	SD	Avr	SD	Avr	SD
GNP-C	0.57	0.121	28.1	5.25	33.8	7.62
GNP-M	[a]	-	28.3	3.25	[a]	-
GNP-M-ox-1:3	0.49	0.552	56.3	25.65	67.1	22.36
GNP-M-ox-1:6	0.93	0.303	57.6	4.7	89.8	19.59

[a] Intensity is too low to fit to model and calculate $I_{(D/G)}$ and also to determine $I_{width(D)}$

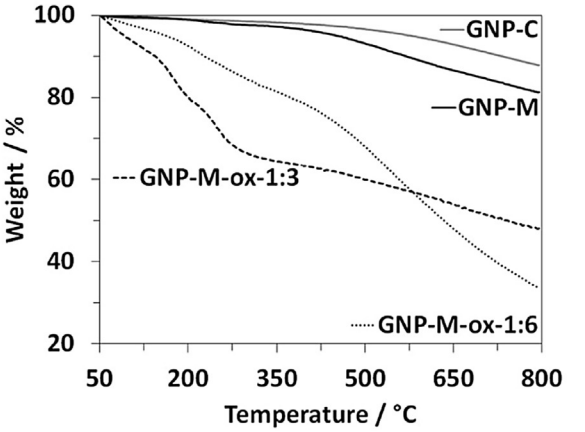

Fig. 4. A) Representative unpolarized Raman spectra for GNP-C, GNP-M, GNP-M-ox-1:3, and GNP-M-ox-1:6 powders, acquired at ambient conditions. B) Intensity ratio of the (D/G) bands of GBMs powders. Results are presented as mean and standard deviation (n = 3). C) TGA curves and weight loss for GBMs powders.

toxic at 24 h for concentrations above 20 μg mL^{-1}. However, cell metabolic activity recovered over time, and at 48 h toxicity is only present above 50 μg mL^{-1}. At 72 h the results show toxicity only slightly above the limit of 70% for 100 μg mL^{-1}. For GNP-M, toxicity occurs at 24 h above 50 μg mL^{-1}. At 48 and 72 h, toxicity is observed above 20 μg mL^{-1}. These results are in agreement with conclusions from our previous review on graphene-based materials (GBMs) biocompatibility, in which most analysed studies reported cell viability decreases inferior to 20% after exposure to GBMs concentrations around 10 μg mL^{-1} during 24 h or longer [23].

GNP-M-ox-1:3 unveils a toxicity profile similar to GNP-M, while GNP-M-ox-1:6 biocompatibility is greatly improved. This occurs because GNP-M-ox-1:3 oxidization was not as uniform as for GNP-M-ox-1:6, which is only slightly toxic (viability ≈ 69%, SD = 5.1%) at 24 h for 100 μg mL^{-1}, however at 48 and 72 h of incubation, no toxicity is observed. Controls performed with materials dispersed in DMEM+ without cells, for all concentrations tested, presented similar values to DMEM+, suggesting that the materials tested did not interfere with fluorescence determinations. Results are also presented in terms of fluorescence intensity values, so that the

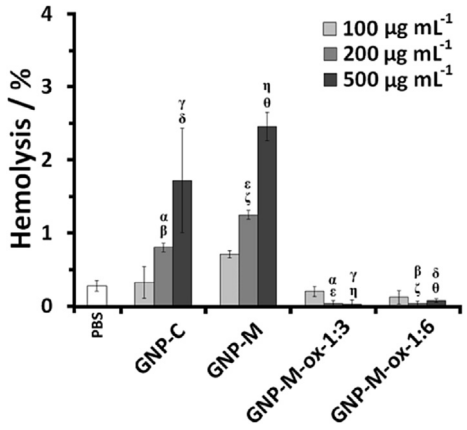

Fig. 5. Percentage of RBCs lysis after 3 h incubation at 37 °C with PBS (negative control), and different concentrations of GBMs (100, 200 and 500 μg mL^{-1}). Positive control (Triton 1% in PBS) resulted in 100% hemolysis. Results are presented as mean and standard deviation (n = 3). Greek symbols represent statistically significant differences between samples within the same concentrations ($p < 0.05$). No significant differences were observed between PBS and GBMs for all concentrations tested ($p > 0.05$).

increase of cell metabolic activity over time can be observed in Fig. S3. It also provides images of the cells incubated with culture medium and GBMs for a concentration of 100 μg mL^{-1}, showing an increase of cell density from 24 to 72 h.

For evaluation of cell proliferation, Ki-67 assay was performed. Ki-67 is a nuclear antigen present at all stages of the cell cycle, except G0 when cells are in the resting state [38,39]. Results presented in Fig. S5 revealed that there is significant decrease in cell proliferation for GNP-C 100 μg mL^{-1} at 24 h comparing with control ($p < 0.05$), followed by a recovery of the proliferative capacity of the cells at 48 h and 72 h. These results are in agreement with the metabolic activity assay obtained for this condition. Importantly, as for the other conditions tested, an increase of cell proliferation has been observed from 24 to 72 h for 50 and 100 μg mL^{-1} concentrations.

Resazurin assay was also performed with HPMEC (Human Pulmonary Microvascular Endothelial Cells). The results showed the same trend as for HFF-1, with GNP-M and GNP-M-ox-1:3 being the most toxic materials, while GNP-M-ox-1:6 showed no toxicity. Also, GNP-C presented initial mild toxicity which was recovered over time. Detailed results are presented as supplementary data in Fig. S7.

Fig. S4 show example images for HFF-1 cells fluorescently labelled for LIVE/DEAD assay. As expected, positive control of cell death (cells incubated with Triton 0.1 wt.% in DMEM+ for 72 h) unveils 100% cell death. Negative control was performed incubating cells with DMEM+, presenting mostly live cells with scarce dead cells.

Fig. 6(B) shows that cell death is below 11% for all materials tested. The resazurin assays showed larger metabolic activity decreases. A possible explanation for this difference is that metabolic activity decreased in some cells, despite possessing intact membranes, avoiding being stained by PI. GNP-M exhibits higher cell death values than GNP-C for all concentrations tested, but no significant differences were observed ($p > 0.05$). However, GNP-C only reveals significantly higher cell death than DMEM+ for 100 μg mL^{-1} ($p < 0.05$), while GNP-M presents it for 20, 50 and 100 μg mL^{-1} ($p < 0.01$), thus exhibiting higher toxicity. Also, GNP-M-ox-1:3 (8%) exhibits similar cell death ($p > 0.05$) to GNP-M (10%) for 100 μg mL^{-1}. However, GNP-M-ox-1:3 is equivalent to DMEM+ bellow this concentration ($p > 0.05$), contrary to GNP-M. GNP-M-ox-1:6 (0%) unveils no cell death for 100 μg mL^{-1}, being similar to

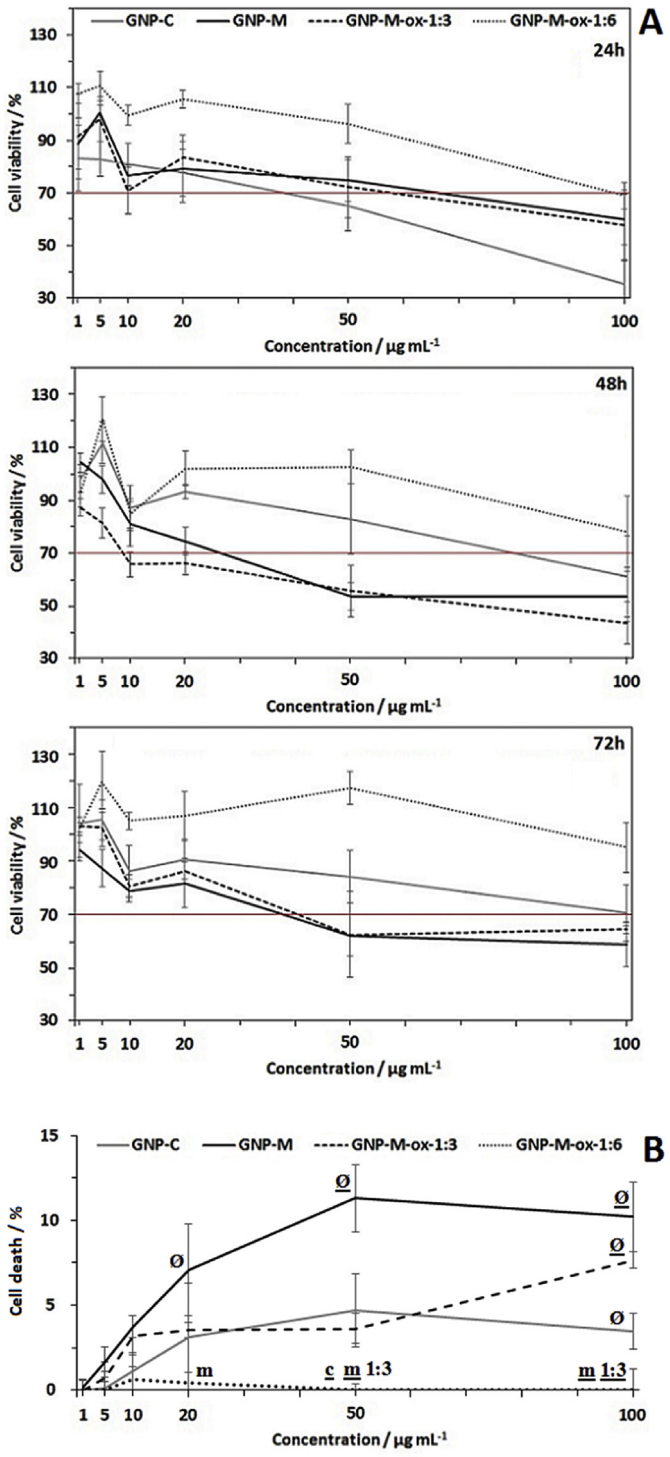

Fig. 6. A) HFF-1 cells viability after incubation with GBMs in DMEM+, at 24, 48 and 72 h. Cell metabolic activity is represented as percentage in comparison with cells cultured in DMEM+ (100%). Results are presented as mean and standard deviation (n = 6). The red line at 70%, marks the toxicity limit, according to ISO 10993-5:2009(E). Statistical analysis is presented in Table S1. B) Percentage of HFF-1 cell death after 72 h of incubation with GBMs. Cell death percentage was corrected by subtraction of the value for cells cultured in DMEM+ (negative control for cell death). Results are presented as mean and standard deviation (n = 3). Statistically significant differences, analysed within each concentration between all GBMs are represented by c – GNP-C, m – GNP-M, 1:3 – GNP-M-ox-1:3 (differences were only found comparing with GNP-M-ox-1:6); Differences comparing with DMEM+ are represented by Ø. Symbols not underlined represent $p < 0.05$, for $p < 0.01$ signs are underlined. (A color version of this figure can be viewed online.)

DMEM+ for all concentrations tested ($p > 0.05$) and significantly less toxic than GNP-M for 20 g mL^{-1} ($p < 0.05$), 50 and 100 μg mL^{-1} ($p < 0.01$). It is also less toxic than GNP-M-ox 1:3 ($p < 0.05$) and GNP-C ($p < 0.01$) for 50 μg mL^{-1}, and GNP-M-ox-1:3 for 100 μg mL^{-1} ($p < 0.01$). These results are in agreement with those observed in the cell metabolic activity assays. The fact that GNP-M-ox-1:6 is homogeneously oxidized, presenting less sharp edges than GNP-M, suggests that less physical damages are induced by oxidized material, explaining the lower number of cell stained with PI and higher cell viability observed in resazurin assay.

Fig. 7, shows that for 10 μg mL^{-1} GNP-C increases ROS production by 2.8 fold, being significantly higher ($p < 0.01$) than GNP-M, GNP-M-ox-1:3 (1 fold) and GNP-M-ox-1:6 (1.6 fold, $p < 0.05$). Also, GNP-M-ox-1:6 is significantly higher than GNP-M and GNP-M-ox-1:3 ($p < 0.05$). For 50 μg mL^{-1}, GNP-C (4.4 fold) induces significantly more ROS production than GNP-M (1.5 fold, $p < 0.05$) and GNP-M-ox-1:6 (1.6 fold, $p < 0.01$).

These results indicate that size is the main factor leading to ROS formation, because smaller GNP-C penetrates cell membrane more easily than GNP-M, GNP-M-ox-1:3, and GNP-M-ox-1:6, inducing higher intracellular ROS formation.

Controls performed with GBMs dispersed in PBS, incubated with CM-H_2DCFHDA in wells without cells, present similar values to PBS only, incubated with the indicator. Thus, GBMs do not interfere in ROS quantification method used.

Mitochondrial membrane potential (MMP) was evaluated for GBMs at concentrations between 10 and 100 μg mL^{-1}, with 48 h incubation. It was observed to be decreased for both GNP-M and GNP-M-ox-1:3 for concentrations above 10 μg mL^{-1} and for GNP-C above 50 μg mL^{-1}. For GNP-M-ox-1:6 no significant differences in MMP were perceptible ($p > 0.05$) comparing with cells cultured in DMEM+. Detailed results are presented in Fig. S6.

3.2.2.2. Cell morphology and interaction with GBMs. After the resazurin assays, cells exposed to 50 μg mL^{-1} of GBMs were stained and observed (at 100 μg mL^{-1} GBMs interfere with staining and images had lower quality). Immunofluorescence images (Fig. 8) show that for toxicity positive control (Triton 0.1% in DMEM+), cells cytoskeleton was disassembled. A control was performed with cells cultured in DMEM+, which exhibited the typical “spindle” like

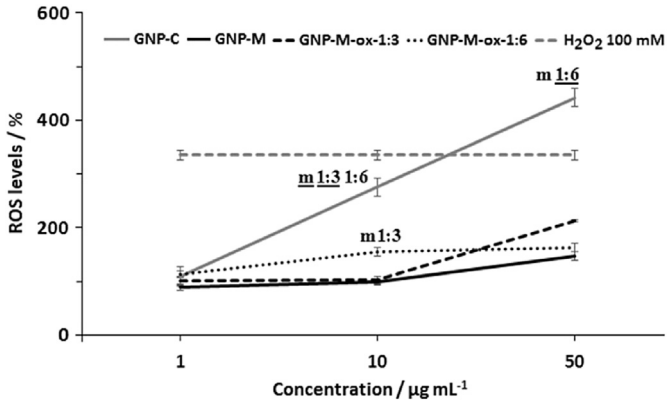

Fig. 7. Intracellular reactive oxygen species levels (ROS) induced by GNP-C, GNP-M, GNP-M-ox-1:3, and GNP-M-ox-1:6 (1, 10, 50 μg mL^{-1}), when incubated with HFF-1 cells for 1 h. Negative control for ROS levels increase is PBS (considered 100%) and positive control H_2O_2 100 mM. Results are presented as mean and standard deviation (n = 3). Statistically significant differences, analysed within each concentration are represented by c – GNP-C, m – GNP-M, 1:3 – GNP-M-ox-1:3, 1:6 – GNP-M-ox-1:6. Symbols represented above a sample concentration indicate that sample is different from samples represented by the symbols for that concentration. Symbols are not underlined when $p < 0.05$ and underlined when $p < 0.01$. Above 10 μg mL^{-1} all samples are different from PBS ($p < 0.01$).

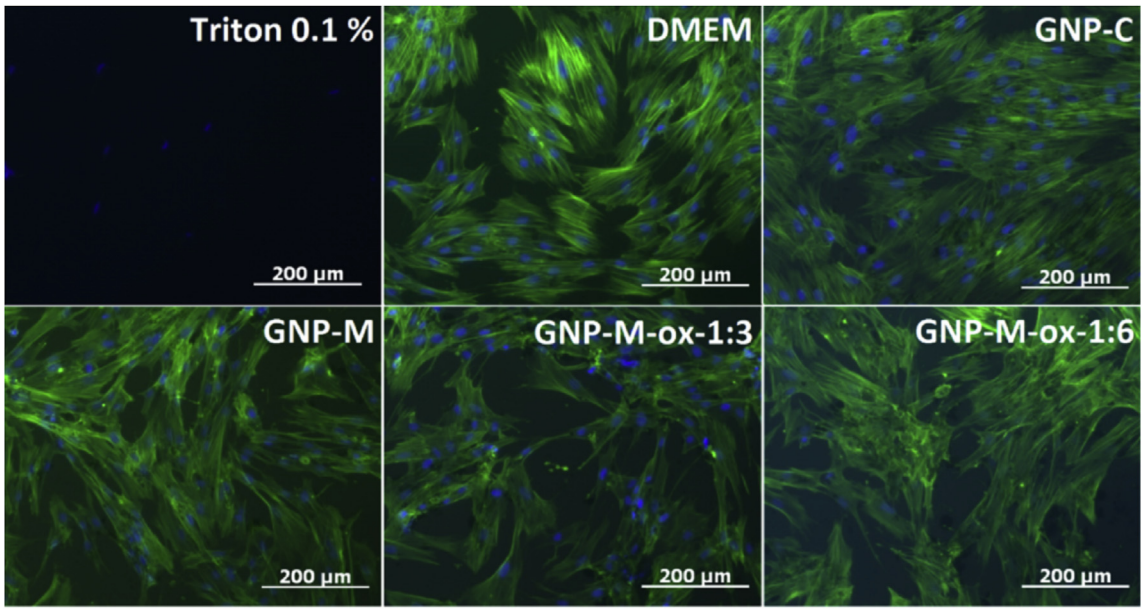

Fig. 8. Representative immunofluorescence images of HFF-1 cells after 72 h incubation with 50 µg mL^{-1} of GNP-C, GNP-M, GNP-M-ox-1:3 and GNP-M-ox-1:6. Triton 0.1% in DMEM+ was used as positive control for changed morphology and cells grown in DMEM+ as negative control. Cells were stained with DAPI (nuclei) – blue and Phalloidin (F-actin in cytoskeleton) – green. Scale bar represents 200 µm. (A color version of this figure can be viewed online.)

shape of fibroblasts. After 72 h of incubation with 50 µg mL^{-1} GNP-C, cells exhibit a normal morphology, similar to negative control. For GNP-M, the cell density is lower, with some cells showing altered morphology and being weakly attached to the bottom of the well. Similar images were obtained for GNP-M-ox-1:3. However, for GNP-M-ox-1:6, cell morphology is normal and similar to cell cultured in DMEM+. As expected, these results are in agreement with those observed in cell viability assays results (see 3.2.2.1) at 72 h for all materials.

TEM images (Fig. 9(B)) show that GNP-C interacts with plasma membrane, being internalized without causing membrane damages, probably by pinocytosis. GNP-C is found often in cytoplasm, being able to interact with mitochondria (Fig. 9(C)), which may induce ROS production (see 3.2.2.1). Sometimes, GNP-M causes cell

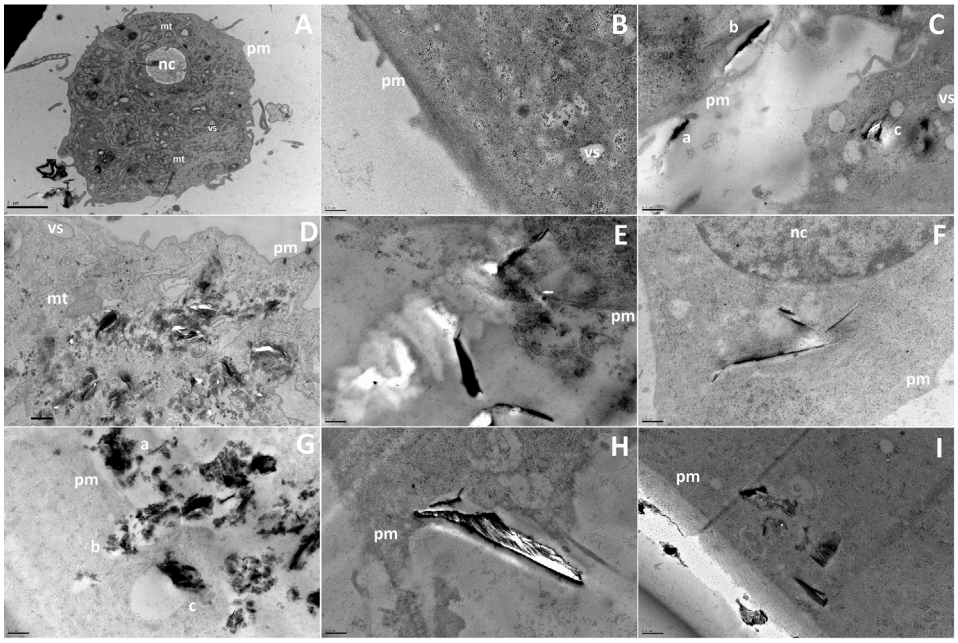

Fig. 9. TEM images of HFF-1 cells incubated for 72 h with 100 µg mL^{-1} GBMs. A, B – DMEM+, C – GNP-C (a – particle interacting with plasma membrane (pm), b – particle internalized and in contact with plasma membrane, c – particle inside a vesicle (vs) in cytoplasm), D – GNP-C particles spread in cytoplasm and interaction with a mitochondria (mt), E – Membrane rupture (white arrow) and cytoplasmic content leakage caused by GNP-M particle, F – GNP-M in cytoplasm (nc – nucleus), G – GNP-M-ox-1:3 (a – interacting with plasma membrane, b – entering through plasma membrane, c – vesicle containing an internalized particle), H – GNP-M-ox-1:6 particle in contact with plasma membrane causing no damages, I – GNP-M-ox-1:6 inside cytoplasm. Scale bar represents 0.5 µm for all images except for image A, in which it represents 2 µm.

membrane damage (Fig. 9(D)), entering cells and being found inside plasma membrane (Fig. 9(E)). However, this seems to be less frequent than for GNP-C. It is not clear if internalization always occurs by membrane rupture or other mechanism. GNP-M-ox-1:3 interacts with plasma membrane, being internalized and forming vesicles in cytoplasm. The internalization process occurs both with and without causing membrane damages (Fig. 9(F)). GNP-M-ox-1:6 was found not to cause membrane damages (Fig. 9(G)), probably do to having less sharp edges. However, it was found inside cells in some cases (Fig. 9(H)). For all materials, the internalized particles had sizes from hundreds of nanometres to 5 μm. Internalized agglomerated particles have therefore not been observed.

4. Discussion

The particle size distribution of GBMs dispersed in water was determined to evaluate their agglomeration state in conditions similar to those used in the biocompatibility assays. After sonication, agglomerated fractions were identified for all materials except GNP-C. The oxidation of GNP-M to GNP-M-ox-1:3 and 1:6 slightly reduced agglomeration, as expected due to increased hydrophilicity. However, it was observed by optical microscopy that over time all materials sediment on the bottom of the wells contacting with the cells. This can be explained by the presence of more oxygen-containing functional groups, allowing hydrogen bonds between GNP particles. Despite agglomerates with considerable size being present, TEM images show that only small platelets and agglomerates, with diameters bellow 5 μm, are internalized.

To our knowledge, a complete characterization of the *in vitro* biological effect of materials oxidized to different degrees, comparing with the base GBM, has not been performed until date. For this reason, the oxidation degree of the materials and the functional groups present were studied with particular attention. GNP-M-ox-1:6 was oxidized in higher extension and more homogeneously than GNP-M-ox-1:3, because of the higher amount of $KMnO_4$ used. Also, more sp^2 disruption is observed for GNP-M-ox-1:6 due to more effective introduction of oxygen-containing functional groups in GNP-M surface. GNP-M-ox-1:3 was preferentially oxidized in platelets edges, because peripheral oxidation demands lower amount of $KMnO_4$. Finally, different amounts of oxygen-containing functional groups were introduced in both materials, GNP-M-ox-1:3 presenting mostly epoxides and carbonyls and GNP-M-ox-1:6 carboxyls and hydroxyls.

No toxicity (0.1% lysis) was caused by both oxidized materials in RBCs, while for the original GNP-M, 2.5% hemolysis occurred after 3 h incubation with high concentrations of 500 μg mL^{-1}. The published literature on this topic is scarce and shows that hemocompatibility is dependent on the particular GBMs considered. Dong et al. observed that functionalization of GO with carboxylic groups improved its hemocompatibility [40]. Sasidharan et al. reported that both pristine bilayer graphene (p-G) obtained by chemical oxidation of graphite and thermal exfoliation, and carboxyl-functionalized graphene (f-G) by mild chemical oxidation were nonhemolytic (hemolysis ≈0.2%) up to a tested concentration of 75 μg mL^{-1} with incubations of 3 h at room temperature [31]. Liao et al. [41] performed hemolysis assays for GO (C at.% 2:1 O at.%) obtained by a MHM from graphite and GS – graphene sheets (C at.% 7:1 O at.%) obtained from GO by hydrothermal treatment. They observed that GO caused about 80% hemolysis and graphene sheets (GS) about 15%, for the higher concentration tested of 200 μg mL^{-1}, for the same incubation time.

Metabolic activity of two cell lines (HFF-1 and HPMEC) exposed to different concentrations of GBMs over time was evaluated. These models were chosen because they are human non-cancerous cell lines, from tissues that may be exposed to GBMs in case of either dermal contact or inhalation, respectively for HFF-1 and HPMEC. To the best of our knowledge, biocompatibility of HPMEC exposed to GBMs has never been reported. The results show similar toxicological profile for GBMs in contact with both cell lines. GNP-M-ox-1:3 causes a decrease of HFF-1 cells metabolic activity similar to the base material GNP-M. However, the more homogeneously oxidized GNP-M-ox-1:6 is biocompatible up to the highest concentration tested (100 μg mL^{-1}). Hong et al. [42] observed that GO (produced by MHM from graphite (1:3 $KMnO_4$), O at.% = 38%, hydrodynamic diameter (HD) = 200 nm) caused a decrease in HeLa cells metabolic activity of about 15% and 25%, respectively for 48 h incubations with 10 and 100 μg mL^{-1}. When this material was re-oxidized by the same method (G2xO – O at.% of 54%, HD = 200 nm), the metabolic activity decreased about 5% and 25% for 10 and 100 μg mL^{-1} (48 h), respectively. Comparing with our work, GO and G2xO are nanometric, while GNP-M, GNP-M-ox-1:3 and 1:6 are in the micrometer range. Thus, the biologic relevance of oxidation may be different.

GNP-M-ox-1:6 causes no metabolic activity decrease, contrary to GNP-M-ox-1:3. With a more extensive and homogeneous oxidation, GNP-M sharp edges fold, by formation of intra-platelet hydrogen bonds, causing much less damage to cell membrane and structures. However, GNP-M-ox-1:6 is also found inside cells, pointing out to a non-disruptive internalization mechanism. These results are in agreement with immunocytochemistry observations of normal cell morphology for GNP-M-ox-1:6, contrarily to GNP-M and GNP-M-ox-1:3. Also, LIVE/DEAD assay shows lower cell death for GNP-M-ox-1:6, comparing with GNP-M. The fact that GNP-M-ox-1:6 causes no damage on cell structure was confirmed by a non-reduced cell metabolic activity at all concentrations, comparing with cells cultured in DMEM+, contrary to GNP-M and GNP-M-ox-1:3, which revealed decreases for concentrations above 10 μg mL^{-1}. Sasidharan et al. [43] observed Vero cells in contact with f-G to have higher cell metabolic activity (comparing to control with culture medium) than the originally toxic hydrophobic material (p-G), which presented a metabolic activity of 60% for a concentration 100 μg mL^{-1} and 24 h incubation. Also, Liao et al. [41] studied the biocompatibility of a hydrophilic and a hydrophobic GBM using human skin fibroblasts. They tested GO with an HD in deionized water of about 0.7 μm and GS with 3 μm. It should be noted that as in our work, the same GBM presented larger HD in the reduced form in relation to the oxidized material, due to agglomeration. Using the WST assay, the metabolic activity values for GO were of 88% and for GS of 20% for 24 h incubations with 50 μg mL^{-1} concentrations. Thus, based on the current studies, it can be concluded that the oxidation of a hydrophobic GBM often improves its biocompatibility. Actually, GNP-M-ox-1:6 has increased metabolic activity, comparing with negative control (cells cultured in DMEM+) at 24 h for 100 μg mL^{-1}, and at 72 h for 50 μg mL^{-1} and above. This suggests a favourable effect on cell proliferation. Such was confirmed by evaluating cell proliferation, which showed to significantly increase ($p < 0.05$), not only for GNP-M-ox-1:6, but for all GBMs at 72 h, for the higher concentration – 100 μg mL^{-1}, comparing with DMEM+. This points out that GNP-M-ox-1:6 is not toxic at higher concentrations, opposing to other GBMs. Interestingly, Ruiz et al. [44] observed that mammalian colorectal adenocarcinoma HT-29 cells attached and proliferated more efficiently in GO coated glass slides, than in control (glass slides).

An interesting aspect that is lacking from existing studies on GBMs biocompatibility has to do with the effect of particle size on the biocompatibility of hydrophobic GBMs. For this reason, biocompatibility tests were also performed for GNP-C, which exhibits smaller size than GNP-M and completely exfoliates in aqueous medium in particles with HDs of about 0.5 and 2 μm. GNP-C seems to lead to lower (1.7%) Hb leakage from RBCs than GNP-M

(2.5%) for 3 h incubation with a high concentration of 500 μg mL^{-1}. However, these differences are not statistically significant ($p > 0.05$). Liau et al. compared the hemolytic activity of GO with different sizes, produced by ultrasounds fragmentation of the base GO. They conclude that after 30 min sonication, GO decreased size by half to about 0.8 μm and caused higher hemolysis than the original material, which was already hemolytic. Liau et al. [41] also observed that no hemolysis was observed after coating the most hemolytic GO with chitosan, due to prevention of toxic interactions of RBCs with materials. Thus, polymer coating is a method that can be tried to improve GBMs biocompatibility.

Higher decreases on cell metabolic activity were observed for GNP-C at 24 h than for GNP-M. However, at 48 and 72 h GNP-M decreases metabolic activity more than GNP-C. This can be explained by GNP-C inducing more ROS production than GNP-M in the initial contact with cells (1 h incubation), causing early toxicity at 24 h, from which cells recover over time. Sasidharan et al. observed highly increased ROS levels in Vero cells for p-G, unfortunately f-G was not tested. However, Liao et al. [41] observed a 9-fold increase (control: cells with no GBMs) in ROS production for GO, comparing to GS (about 1.3 fold). For GNP-M, metabolic activity decreases with incubation time, because physical damages are caused on cell membranes, by the platelets' sharp edges. LIVE/DEAD results show that GNP-M causes 3-fold more cell death than GNP-C. Additionally, immunocytochemistry images show that cells incubated with GNP-C display normal cell morphology, as opposed to cells incubated with GNP-M. In fact, the latter particles were found to cause cell membrane rupture by TEM. GNP-C particles, on the other hand, were found inside cells, in higher quantities, without evidence of damages, despite an observed occurrence of interaction with cell membrane. To our knowledge it is the first time different types of GBMs interaction, internalization and effects in non-phagocytic or cancer line cells is shown in TEM images. Lamel et al. [25] observed that graphene oxide (GO) and carboxyl graphene nanoplatelets (CXYG) penetrate through the plasma membrane of Hep G2 (human hepatocellular carcinoma) cells into the cytosol, are concentrated and encapsulated in intracellular vesicles. They also observed that exposure to GO (HD ≈ 0.4 μm) and CXYG (HD ≈ 1.7 μm) nanoplatelets results in high intracellular ROS levels by perturbation of mitochondrial structure and function. GNP-C (HD ≈ 0.5 and 2 μm) caused high increases of ROS levels and was found spread in cytoplasm close to mitochondria. However, as mentioned above, this material did not cause membrane damages. GNP-M-ox-1:6, which was internalized, did not cause observable membrane damages, despite having a particle size distribution around 35 μm. It must be noted, however, that only particles bellow 5 μm were found in cytoplasm for all materials tested.

Since GNP-C induces higher ROS production than the other materials and was found close to mitochondria, mitochondrial membrane potential (MMP) was evaluated. However, since a decrease on MMP was observed not only for GNP-C, but also for GNP-M and GNP-M-ox-1:3, another mechanism besides ROS formation is involved in MMP decrease, such as direct mitochondrial damage. Lamel et al. [25] also proposed that MMP disruption can be caused by physical interaction with mitochondria, besides being induced indirectly through ROS resultant from GBMs bio-interaction. The collapse of the MMP coincides with the opening of the mitochondrial permeability transition pores, leading to the release of cytochrome c into the cytosol, which in turn triggers other downstream events in the apoptotic cascade [45]. MMP is decreased for both GNP-M and GNP-M-ox-1:3 for concentrations above 10 μg mL^{-1} and for GNP-C above 50 μg mL^{-1}, pointing out apoptosis induced by these GBMs. For GNP-M-ox-1:6 no significant differences in MMP were perceptible ($p > 0.05$) comparing with cells cultured in DMEM+. These results are in agreement with above discussed data regarding cell death (LIVE/DEAD assay).

5. Conclusion

The biocompatibility of GNPs with different platelet sizes and oxidation degrees was evaluated *in vitro*. GNP-C, which exhibited smaller sizes, was shown to be generally more biocompatible than GNP-M. The sharper and longer edges of GNP-M platelets cause membrane damages on cells being cytotoxic above 20 μg mL^{-1}. GNP-C, despite being internalized without causing membrane damages, increases ROS levels being toxic above 50 μg mL^{-1}.

The complete oxidation of GNP-M (GNP-M-ox-1:6) folds its sharp edges, assuring biocompatibility until the highest concentration tested (100 μg mL^{-1}). GNP-M-ox-1:6 has an oxygen content of 24% (mostly carboxyls and hydroxyls) and is dispersible in water by sonication, revealing potential to be used for biomedical purposes.

Generally, oxidation was found to be more important than size, since more oxidized GNP-M performed better than smaller GNP-C.

Acknowledgements

Artur Pinto wishes to thank Fundação para a Ciência e a Tecnologia (FCT) for PhD grant SFRH/BD/86974/2012, funded by European Social Fund and Portuguese Ministry of Education and Science (MEC) through Programa Operacional Capital Humano (POCH).

Authors wish to thank Rui Fernandes and Francisco Figueiredo from the Histology and Electron Microscopy Service (HEMS) of IBMC, Porto, for the assistance in TEM studies, André Maia from Advanced Light Microscopy Screening Center of IBMC, for the assistance in In cell analyser studies, Rui Rocha for the assistance in scanning electron microscopy studies at CEMUP, Porto, the Imunohemotherapy Service of Hospital S. João, Porto, for providing buffy coats, and Tiago Duarte from IBMC for providing ROS reagent.

This work was funded by project PEst-C/SAU/LA0002/2013 and by project UID/EQU/00511/2013-LEPABE (Laboratory for Process Engineering, Environment, Biotechnology and Energy – EQU/00511) by FEDER funds through Programa Operacional Competitividade e Internacionalização – COMPETE2020 and by national funds through FCT.

Appendix A. Supplementary data

Supplementary data related to this article can be found at http://dx.doi.org/10.1016/j.carbon.2015.11.076.

References

[1] M.J. Allen, V.C. Tung, R.B. Kaner, Honeycomb carbon: a review of graphene, Chem. Rev. 110 (1) (2010) 132–145.
[2] M. Batzill, The surface science of graphene: metal interfaces, CVD synthesis, nanoribbons, chemical modifications, and defects, Surf. Sci. Rep. 67 (3–4) (2012) 83–115.
[3] W. Choi, I. Lahiri, R. Seelaboyina, Y.S. Kang, Synthesis of graphene and its applications: a review, Crit. Rev. Solid State 35 (1) (2010) 52–71.
[4] H. Kim, A.A. Abdala, C.W. Macosko, Graphene/polymer nanocomposites, Macromolecules 43 (16) (2010) 6515–6530.
[5] K.P. Loh, Q.L. Bao, P.K. Ang, J.X. Yang, The chemistry of graphene, J. Mater Chem. 20 (12) (2010) 2277–2289.
[6] O.V. Prezhdo, P.V. Kamat, G.C. Schatz, Virtual issue: graphene and functionalized graphene, J. Phys. Chem. C 115 (8) (2011) 3195–3197.
[7] C.N.R. Rao, K.S. Subrahmanyam, H.S.S.R. Matte, U. Maitra, K. Moses, A. Govindaraj, Graphene: synthesis, functionalization and properties, Int. J. Mod. Phys. B 25 (30) (2011) 4107–4143.
[8] V. Singh, D. Joung, L. Zhai, S. Das, S.I. Khondaker, S. Seal, Graphene based materials: past, present and future, Prog. Mater Sci. 56 (8) (2011) 1178–1271.
[9] R.J. Young, I.A. Kinloch, L. Gong, K.S. Novoselov, The mechanics of graphene nanocomposites: a review, Compos Sci. Technol. 72 (12) (2012) 1459–1476.
[10] O.C. Compton, S.T. Nguyen, Graphene oxide, highly reduced graphene oxide,

and graphene: versatile building blocks for carbon-based materials, Small 6 (6) (2010) 711–723.
[11] D.R. Dreyer, S. Park, C.W. Bielawski, R.S. Ruoff, The chemistry of graphene oxide, Chem. Soc. Rev. 39 (1) (2010) 228–240.
[12] J. Kim, L.J. Cote, J.X. Huang, Two dimensional soft material: new faces of graphene oxide, Accounts Chem. Res. 45 (8) (2012) 1356–1364.
[13] J.I. Paredes, S. Villar-Rodil, A. Martinez-Alonso, J.M.D. Tascon, Graphene oxide dispersions in organic solvents, Langmuir 24 (19) (2008) 10560–10564.
[14] Y. Zhu, D.K. James, J.M. Tour, New routes to graphene, graphene oxide and their related applications, Adv. Mater. 24 (36) (2012) 4924–4955.
[15] Y.W. Zhu, S. Murali, W.W. Cai, X.S. Li, J.W. Suk, J.R. Potts, et al., Graphene and graphene oxide: synthesis, properties, and applications, Adv. Mater. 22 (35) (2010) 3906–3924. http://onlinelibrary.wiley.com/doi/10.1002/adma.201001068/abstract.
[16] H. Bai, C. Li, G.Q. Shi, Functional composite materials based on chemically converted graphene, Adv. Mater. 23 (9) (2011) 1089–1115.
[17] J.H. Du, H.M. Cheng, The fabrication, properties, and uses of graphene/polymer composites, Macromol. Chem. Phys. 213 (10–11) (2012) 1060–1077.
[18] X. Huang, Z.Y. Yin, S.X. Wu, X.Y. Qi, Q.Y. He, Q.C. Zhang, et al., Graphene-based materials: synthesis, characterization, properties, and applications, Small 7 (14) (2011) 1876–1902.
[19] T. Kuila, S. Bose, A.K. Mishra, P. Khanra, N.H. Kim, J.H. Lee, Chemical functionalization of graphene and its applications, Prog. Mater Sci. 57 (7) (2012) 1061–1105.
[20] K. Yang, S.A. Zhang, G.X. Zhang, X.M. Sun, S.T. Lee, Z.A. Liu, Graphene in mice: ultrahigh in vivo tumor uptake and efficient photothermal therapy, Nano Lett. 10 (9) (2010) 3318–3323.
[21] V.C. Sanchez, A. Jachak, R.H. Hurt, A.B. Kane, Biological interactions of graphene-family nanomaterials: an interdisciplinary review, Chem. Res. Toxicol. 25 (1) (2012) 15–34.
[22] H. Shen, L.M. Zhang, M. Liu, Z.J. Zhang, Biomedical applications of graphene, Theranostics 2 (3) (2012) 283–294.
[23] A.M. Pinto, I.C. Goncalves, F.D. Magalhaes, Graphene-based materials biocompatibility: a review, Colloid Surf. B 111 (2013) 188–202.
[24] A.M. Pinto, J. Cabral, D.A.P. Tanaka, A.M. Mendes, F.D. Magalhaes, Effect of incorporation of graphene oxide and graphene nanoplatelets on mechanical and gas permeability properties of poly(lactic acid) films, Polym. Int. 62 (1) (2013) 33–40.
[25] T. Lammel, P. Boisseaux, M.L. Fernandez-Cruz, J.M. Navas, Internalization and cytotoxicity of graphene oxide and carboxyl graphene nanoplatelets in the human hepatocellular carcinoma cell line Hep G2, Part Fibre Toxicol. 10 (2013).
[26] S. Jaworski, E. Sawosz, M. Grodzik, A. Winnicka, M. Prasek, M. Wierzbicki, et al., In vitro evaluation of the effects of graphene platelets on glioblastoma multiforme cells, Int. J. Nanomed. 8 (2013) 413–420.
[27] K. Kalaitzidou, H. Fukushima, L.T. Drzal, Mechanical properties and morphological characterization of exfoliated graphite-polypropylene nanocomposites, Compos Part A Appl. Sci. Manuf. 38 (7) (2007) 1675–1682.
[28] W.X. Li, Z.W. Xu, L. Chen, M.J. Shan, X. Tian, C.Y. Yang, et al., A facile method to produce graphene oxide-g-poly(L-lactic acid) as an promising reinforcement for PLLA nanocomposites, Chem. Eng. J. 237 (2014) 291–299.
[29] J.A. Moreira, A. Almeida, M.R. Chaves, M.L. Santos, P.P. Alferes, I. Gregora, Raman spectroscopic study of the phase transitions and pseudospin phonon coupling in sodium ammonium sulphate dihydrate, Phys. Rev. B 76 (17) (2007).
[30] C. Monteiro, M. Fernandes, M. Pinheiro, S. Maia, C.L. Seabra, F. Ferreira-da-Silva, et al., Antimicrobial properties of membrane-active dodecapeptides derived from MSI-78, Biochim. Biophys. Acta Biomembr. 1848 (5) (2015) 1139–1146.
[31] A. Sasidharan, L.S. Panchakarla, A.R. Sadanandan, A. Ashokan, P. Chandran, C.M. Girish, et al., Hemocompatibility and macrophage response of pristine and functionalized graphene, Small 8 (8) (2012) 1251–1263.
[32] B. Lesiak, L. Stobinski, A. Malolepszy, M. Mazurkiewicz, L. Kover, J. Toth, Preparation of graphene oxide and characterisation using electron spectroscopy, J. Electron Spectrosc. 193 (2014) 92–99.
[33] A.C. Ferrari, Raman spectroscopy of graphene and graphite: disorder, electron-phonon coupling, doping and nonadiabatic effects, Solid State Commun. 143 (1–2) (2007) 47–57.
[34] M.A. Pimenta, G. Dresselhaus, M.S. Dresselhaus, L.G. Cancado, A. Jorio, R. Saito, Studying disorder in graphite-based systems by Raman spectroscopy, Phys. Chem. Chem. Phys. 9 (11) (2007) 1276–1291.
[35] O.J. Yoon, C.Y. Jung, I.Y. Sohn, H.J. Kim, B. Hong, M.S. Jhon, et al., Nanocomposite nanofibers of poly(D, L-lactic-co-glycolic acid) and graphene oxide nanosheets, Compos Part A Appl. Sci. Manuf. 42 (12) (2011) 1978–1984.
[36] A. Ganguly, S. Sharma, P. Papakonstantinou, J. Hamilton, Probing the thermal deoxygenation of graphene oxide using high-resolution in situ X-ray-based spectroscopies, J. Phys. Chem. C 115 (34) (2011) 17009–17019.
[37] K. Haubner, J. Murawski, P. Olk, L.M. Eng, C. Ziegler, B. Adolphi, et al., The route to functional graphene oxide, Chemphyschem 11 (10) (2010) 2131–2139.
[38] J.M. Hillegass, A. Shukla, S.A. Lathrop, M.B. MacPherson, N.K. Fukagawa, B.T. Mossman, Assessing nanotoxicity in cells in vitro, Wires Nanomed Nanobi 2 (3) (2010) 219–231.
[39] S.C. Patel, G. Lalwani, K. Grover, Y.X. Qin, B. Sitharaman, Fabrication and cytocompatibility of in situ crosslinked carbon nanomaterial films, Sci. Rep. U. K. 5 (2015).
[40] D. Xu, N.L. Zhou, J.A. Shen, Hemocompatibility of carboxylic graphene oxide, Chem. J. Chin. Univ. 31 (12) (2010) 2354–2359.
[41] K.H. Liao, Y.S. Lin, C.W. Macosko, C.L. Haynes, Cytotoxicity of graphene oxide and graphene in human erythrocytes and skin fibroblasts, Acs Appl. Mater. Inter. 3 (7) (2011) 2607–2615.
[42] B.J. Hong, O.C. Compton, Z. An, I. Eryazici, S.T. Nguyen, Successful stabilization of graphene oxide in electrolyte solutions: enhancement of biofunctionalization and cellular uptake, Acs Nano 6 (1) (2012) 63–73.
[43] A. Sasidharan, L.S. Panchakarla, P. Chandran, D. Menon, S. Nair, C.N.R. Rao, et al., Differential nano-bio interactions and toxicity effects of pristine versus functionalized graphene, Nanoscale 3 (6) (2011) 2461–2464.
[44] O.N. Ruiz, K.A.S. Fernando, B.J. Wang, N.A. Brown, P.G. Luo, N.D. McNamara, et al., Graphene oxide: a nonspecific enhancer of cellular growth, Acs Nano 5 (10) (2011) 8100–8107.
[45] E. Gottlieb, S.M. Armour, M.H. Harris, C.B. Thompson, Mitochondrial membrane potential regulates matrix configuration and cytochrome c release during apoptosis, Cell Death Differ. 10 (6) (2003) 709–717.